Premelting at Defects Within Bulk Colloidal Crystals

A. M. Alsayed,[1] M. F. Islam,[1] J. Zhang,[1] P. J. Collings,[1,2] A. G. Yodh[1]*

Premelting is the localized loss of crystalline order at surfaces and defects at temperatures below the bulk melting transition. It can be thought of as the nucleation of the melting process. Premelting has been observed at the surfaces of crystals but not within. We report observations of premelting at grain boundaries and dislocations within bulk colloidal crystals using real-time video microscopy. The crystals are equilibrium close-packed, three-dimensional colloidal structures made from thermally responsive microgel spheres. Particle tracking reveals increased disorder in crystalline regions bordering defects, the amount of which depends on the type of defect, distance from the defect, and particle volume fraction. Our observations suggest that interfacial free energy is the crucial parameter for premelting in colloidal and atomic-scale crystals.

The importance of melting in nature can hardly be overestimated, and yet a detailed understanding of the mechanisms that drive this transformation is still evolving. Scientists have speculated for more than a century about how crystalline solids melt (*1*–*3*). In the process, they have generated microscopic models emphasizing the role of lattice vibrations (*4*, *5*), dislocations (*6*, *7*), grain boundaries (*8*, *9*), surfaces (*10*–*14*), dimensionality (*15*), and combinations thereof. In contrast to the continuous transitions that arise in ferromagnetism and liquid-vapor systems, a first-principle theory of the solid-liquid transition is difficult to derive because of long-range many-body effects, symmetry, and a lack of universality. Furthermore, experimental investigations to test underlying theoretical assumptions are extraordinarily difficult, because they must track motions of individual atoms or defects within crystals. Nevertheless, recent experiments (*16*, *17*) and theory (*18*) have shown that atomic crystal surfaces at equilibrium below the bulk melting point often form melted layers. This premelting lowers the energy barrier for liquid nucleation and effectively prevents superheating of the solid (*16*, *19*).

Many theories have suggested that a similar premelting should occur at defects such as grain boundaries, stacking faults, and dislocations located within the bulk crystal, but these effects have not been observed. Simulations of grain boundaries (*20*, *21*), for example, have found that the free energy of the solid-solid interface can be larger than two solid-liquid interfaces, thereby favoring premelting near the grain boundary. In this work, we imaged the motions of particles in three-dimensional (3D) colloidal crystals during the melting process. The images reveal premelting near grain boundaries and dislocations. Furthermore, particle tracking enabled us to quantify the spatial extent of local particle fluctuations near a variety of defects, as well as within the more ordered parts of the crystal.

Increased disorder was observed in crystalline regions bordering the defects as a function of defect type (e.g., grain boundaries, dislocations, and vacancies), distance from the defect, and particle volume fraction. These observations answer longstanding fundamental questions about melting mechanisms, suggest that grain boundary and dislocation premelting are important effects in the melting process, and introduce new quantitative measures of local disorder. Besides their intrinsic importance for colloid science and technology, all indications suggest that interfacial free energy is the crucial parameter for premelting. Thus, these results are also relevant for atomic-scale materials.

The colloidal crystals used for these studies were equilibrium systems composed of micrometer-sized, nearly hard-sphere particles (*22*). At a high volume fraction, these particles are driven entropically to condense into close-packed crystalline solids (*23*, *24*). A key feature of these measurements is our use of microgel particles (*25*, *26*), whose diameters depend on temperature. Thus, by slightly changing the sample temperature, we precisely vary the volume fraction of particles in the crystal over a significant range, driving the crystal from close packing toward its melting point at a lower volume fraction.

Particle synthesis. The temperature-sensitive colloidal particles required for this investigation were synthesized by free-radical polymerization of *N*-isopropylacrylamide (NIPA) and 2-aminoethyl-methacrylate hydrochloride (AEMA) and cross linked with *N*,*N*′-methylene-bisacrylamide in a buffer solution (pH = 4.0, 50 mM acetic acid) (*27*). The resultant particles were centrifuged down and resuspended in a different buffer solution (pH = 8.3, 0.1 M sodium bicarbonate).

Succinimidyl ester (TAMRA), which is a fluorophore that reacts with the AEMA amine group 5-(6)-carboxytetramethylrhodamine, was added to the preparation solution for fluorescence studies that are not reported here. The microgel particles with TAMRA became slightly smaller in size, but the presence or absence of TAMRA changed the phase behavior of the suspension only slightly.

The particles were then cleaned cyclically, by first concentrating them with centrifugation and then resuspending them in a buffer solution (pH = 4.0, 20 mM acetic acid). Finally, in order to minimize particle aggregates, the suspensions were centrifuged for a few minutes, the supernatant was collected, and the process was repeated (~10 times). For temperatures below 32°C, NIPA solubility increases with decreasing temperature. Consequently, the NIPA-AEMA particle diameter varies in our experimental temperature regime (20° to 28°C) as a result of water moving into and out of the microgel. The particles made from NIPA-AEMA copolymer have higher surface charge and are more stable against aggregation in solution during processing than are particles made from pure NIPA. Counterions in the buffer solution ensure that the charges on the particles are screened. In addition, the polymerization rate in our acidic solutions (pH = 4.0) was slow, resulting in reduced size polydispersity. Dynamic light-scattering measurements at 25°C determined the particle radius to be ~375 nm, with a polydispersity less than 3%.

Microscopy and temperature control. Experimental observations were made with an upright microscope (Leica DMRXA2) equipped with a 12-bit monochrome cooled camera (QImaging RETIGA) and a motorized stage. The dimensions of the sample chamber were 18 mm by 4 mm by 0.1 mm. The temperature of the sample and objective lens (magnification ×100, 1.4 numerical aperture) were controlled to within 0.1°C and were increased in 0.1°C increments. Samples were left to equilibrate at each temperature for 1 hour. In order to track premelted regions and defects, we took bright-field video images for 0.6 s at 100-nm intervals throughout the ~100-μm-thick chamber. Because the microgel particles were ~95% water, their refractive index was very close to that of water, allowing us to obtain high-quality images throughout the sample volume. In order to track individual particle movement, we used a video shutter time of 2 ms. Image fields were chosen to contain ~400 particles, and particle positions were determined at resolutions much smaller than the particle radius or crystal lattice constant

[1]Department of Physics and Astronomy, University of Pennsylvania, 209 South 33rd Street, Philadelphia, PA 19104–6396, USA. [2]Department of Physics and Astronomy, Swarthmore College, Swarthmore, PA 19081–1397, USA.

*To whom correspondence should be addressed. E-mail: yodh@physics.upenn.edu

(*28*). Fifteen minutes of video were recorded at each temperature.

Sample preparation. The particle suspensions were loaded into the chamber using capillary forces at 28°C; i.e., just below the melting temperature. In this process, the suspension was sheared. Initially we found that well-oriented face-centered cubic (fcc) crystals grew from the glass coverslip surfaces and that the middle of the sample was fluid-like. After loading, we annealed the sample at 28°C for 24 hours, during which the samples crystallized. Bragg diffraction (Fig. 1, inset) from various parts of the annealed sample, measured in the microscope with a Bertran lens, exhibited no detectable change in peak positions. The crystal had very few defects close to the glass walls. We never observed premelting near the walls; it is possible the walls stabilized the crystal or that the (111) planes near the wall surfaces were intrinsically stable (*19*). Interior crystalline regions had many more defects. A few defects in the sample interior are shown in Figs. 2 and 3. Most of the defects we observed were stacking faults, which caused the formation of partial dislocations (Fig. 3) (*29*). We also observed vacancies. Typically, the crystals lost their preferential orientation after melting and recrystallization, displaying large crystalline regions with different orientations separated by grain boundaries (Fig. 2).

Premelting from grain boundaries. One of the common melting mechanisms exhibited by our colloidal crystals is illustrated in Fig. 2. The figure shows a small-angle (~13°) grain boundary. The grain boundary is composed of an array of dislocations, one of which is shown in the inset of Fig. 2A. The number of particle nearest neighbors along the grain boundary varies from five to seven (red and blue particles in the inset). These packing mismatches create stress in the crystal near the grain boundary. The dashed line in Fig. 2A shows a Shockley partial dislocation that continues into the grain boundary. The region to the right of the dashed line is out of focus, and the particles in this portion of the image appear darker than average, whereas the region to the left is in focus and the particles appear whiter than average.

Figure 2B shows the same region at higher temperature (lower particle volume fraction). In order to minimize the interfacial free energy caused by stress and surface tension, particles near the grain boundary start to premelt. The inset of Fig. 2B shows these particles jumping rapidly from one site to another. In contrast, melting is not observed near the partial dislocation (dashed line); its interfacial free energy is apparently less than that of the grain boundary. In Fig. 2C, the temperature is slightly higher and melting has erupted along the grain boundary. At this stage, the sample volume fraction is higher than the bulk melting particle volume fraction, and the melted region has engulfed the partial dislocation. The width of the premelted region continues to increase as the temperature is raised from 28.0° to 28.2°C (Fig. 2, B to D).

Premelting from dislocations. In addition to grain boundary premelting, the colloidal crystals display premelting from partial dislocations (Fig. 3). This effect is more apparent when the grain boundaries are relatively far from the partial dislocations. Figure 3, A and B, show images of the 61st layer (green) and the 62nd layer (red and yellow), respectively, of the colloidal crystal at 25.0°C.

Figure 3C shows a superposition of these layers. Both of these layers represent (111) planes in the crystal. The Burger's circuit in the 61st layer (green) yields a zero Burger's vector, indicating no defect in the layer. Because a dislocation is present in the next layer, some of the particles are slightly out of focus. The Burger's circuit for the 62nd layer (yellow) reveals a Shockley partial dislocation with a Burger's vector of $\frac{1}{6}(\bar{1}\bar{1}2)$ (*29*). The inset contains a 3D illustration of the Shockley dislocation, showing the 61st layer and the undisplaced particles in the 62nd to 64th layers in green and the displaced particles in the 62nd to 64th layers in yellow.

In monodisperse nearly hard-sphere colloidal crystals, the difference in the energy between fcc and hexagonal close-packed (hcp) structures is very small (*30*, *31*) and stacking faults are common (*32*). Shockley partial dislocations arise as a result of these stacking faults. Face-centered cubic crystals stack in the pattern ABCABC along the (111) direction, and hcp crystals stack in the pattern ABAB. The green particles in Fig. 3A are in the A positions, whereas the red and yellow particles are in the B and C positions of the next layer, respectively. This stacking fault opens up gaps between the two close-packed structures within the crystal (two gaps are visible in the image and make an

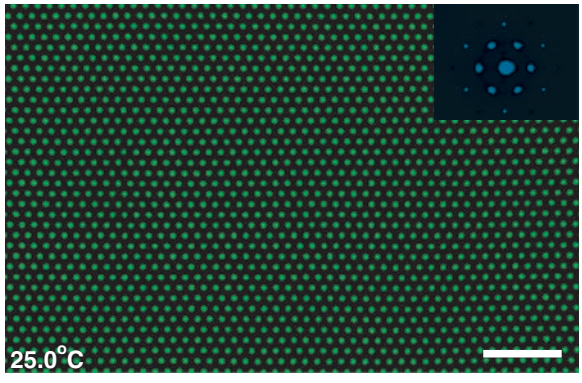

Fig. 1. Bright-field image of the NIPA particle colloidal crystal showing no defects; the slice is of the seventh layer from the coverslip. Each bright spot corresponds to the central region of a 0.75-μm-diameter particle. Because of sample preparation and annealing, the primary defects are partial dislocations that exist in the interior of the crystal. Scale bar, 5 μm. (Inset) Bragg diffraction (wavelength = 405 nm) of the same sample.

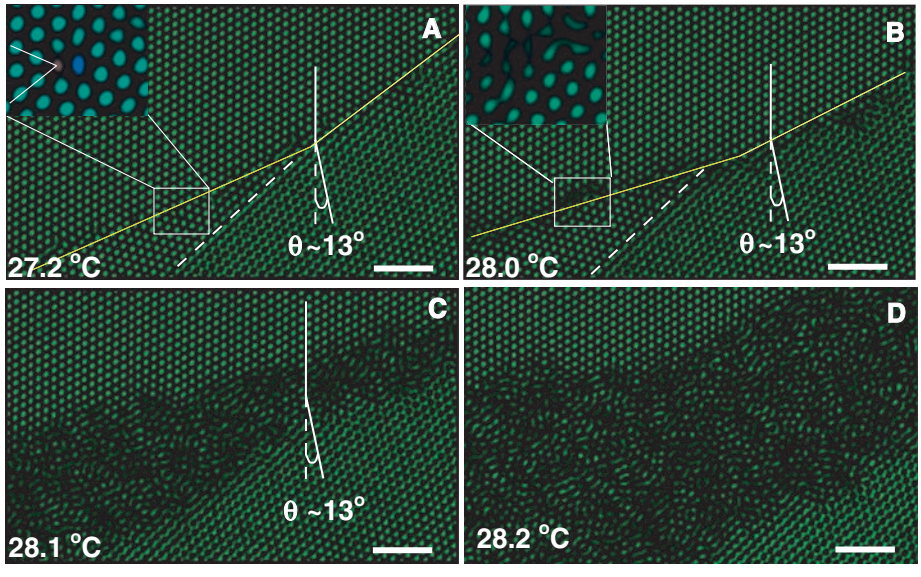

Fig. 2. Premelting of the colloidal crystal at a grain boundary. The figure shows bright-field images at different temperatures (i.e., particle volume fractions) of two crystallites separated by a grain boundary (crystallites tilted at an angle θ ~ 13° with respect to one another). (**A**) Sample at 27.2°C. The solid and dashed lines show the grain boundary and a partial dislocation, respectively. The grain boundary cuts the two crystals along two different planes (the yellow line has two slopes). It is composed of an array of dislocations; the two extra planes are indicated by lines in the inset. (**B**) Sample at 28.0°C. The grain boundary starts to premelt; nearby particles undergo liquid-like diffusion (inset). The partial dislocation, denoted by the dashed line, is not affected. (**C** and **D**) The same sample at 28.1° and 28.2°C, respectively. The width of the premelt region near the grain boundary increases. Scale bars, 5 μm.

angle of 120°C with respect to one another). Nearby particles fluctuate into and out of these gaps. The angle the gaps make with the (111) plane suggests that the gaps cut the crystal along (100) planes, as shown in the 3D illustration. Finally, Fig. 3D shows the 62nd crystal layer at 28.2°C. At this temperature, which is higher than the grain boundary premelting temperature, the crystal has begun to premelt from the partial dislocation.

Positional fluctuations. Using the Lindemann parameter L, which is a measure of the particle mean square fluctuation, we have quantified these observations as a function of sample temperature and volume fraction (Fig. 4). Inset 1 shows the time evolution of mean square displacement (MSD) for particles in the bulk crystal at three different temperatures. On short time scales, the MSD exhibits free particle diffusion; on long time scales, the particles are caged by nearest neighbors and the MSD asymptotically approaches a constant. This asymptotic constant corresponds to twice the variance of the particle's displacement from its equilibrium position (*33*, *34*). We computed the 3D L by using the measured 2D MSD and assuming that particle fluctuations were isotropic. We used the relation $L = \frac{1}{r_{nn}}\sqrt{\frac{3}{4}\langle r^2(\tau \to \infty)\rangle}$, where r_{nn} is the crystal nearest-neighbor distance, and $\langle r^2\ (\tau \to \infty)\rangle$ is the asymptotic value of the 2D particle MSD.

In the main plot of Fig. 4A, L experiences a change in slope at 24.7°C. At this temperature, the hydrodynamic diameter of the particles as measured by dynamic light scattering is ~754 nm (inset 2), and the nearest-neighbor distance derived from pair correlation functions measured by microscopy is ~750 nm. Thus, at this temperature, it is reasonable to assume that the particles are close packed with a volume fraction of ~0.74. Below this temperature, the particle motions are constrained, and L varies less strongly with temperature. With this assumption, we can deduce the particle number density. This number density and the measured hydrodynamic radius (inset 2) determine the particle volume fraction as a function of temperature (upper scale of Fig. 4A). The crystal appears to melt at a particle volume fraction of ~0.54, which is close to the hard-sphere prediction of 0.545 (*24*). The lattice constant in the solid regions, derived from our measurements of the particle pair correlation functions, also decreases sharply near this volume fraction. Although our particles are not perfect hard spheres (*22*), the melting point suggests that they may be approximated reasonably well as such.

The Lindemann melting criterion, which predicts melting for $L \sim 1/8$ (*4*), continues to provide a useful benchmark nearly 100 years after it was originally suggested. The data for L in Fig. 4A are taken from deep within the crystalline regions of the sample, below the melting point. At 28.3°C, the sample begins to melt, and a coexistence of liquid and solid domains is observed. In Fig. 4B, we show local measurements of L near various crystalline defects and near the premelt boundary just before bulk melting (28.3°C). We find that the particle fluctuations in the proximity of these regions are measurably larger than those in the bulk crystal. Furthermore, we find that the magnitude of these fluctuations decreases approximately exponentially as the measurement position is translated away from the premelt region toward the interior of the bulk crystal. Extrapolation of our exponential fits of L to zero distance suggest that $L \sim 0.18$ in the premelt region, twice its interior value of ~0.085 at the same temperature. Evidently, the greater number of vacancies in the premelted region increases the free volume for particle

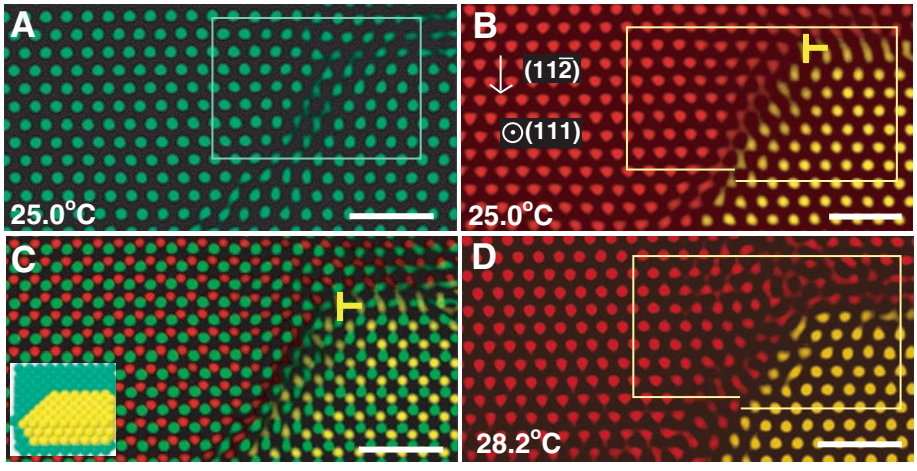

Fig. 3. Melting of a colloidal crystal initiated at a Shockley partial dislocation in the absence of grain boundaries. (**A** and **B**) Bright-field images of the 61st and 62nd layers at 25.0°C, respectively. Colloidal particles fluctuate more in the 62nd layer because of the gap created by the dislocation. (**C**) Superposition of 61st (green) and 62nd (red and yellow) layers. The image shows particles in positions A (green), B (red), and C (yellow). (Inset) 3D illustration of the 61st to 64th layers (bottom to top) showing the displacement of the yellow spheres in the 62nd to 64th layers. (**D**) 62nd layer at 28.2°C, where the crystal starts to premelt at the dislocation. Scale bars, 3 μm.

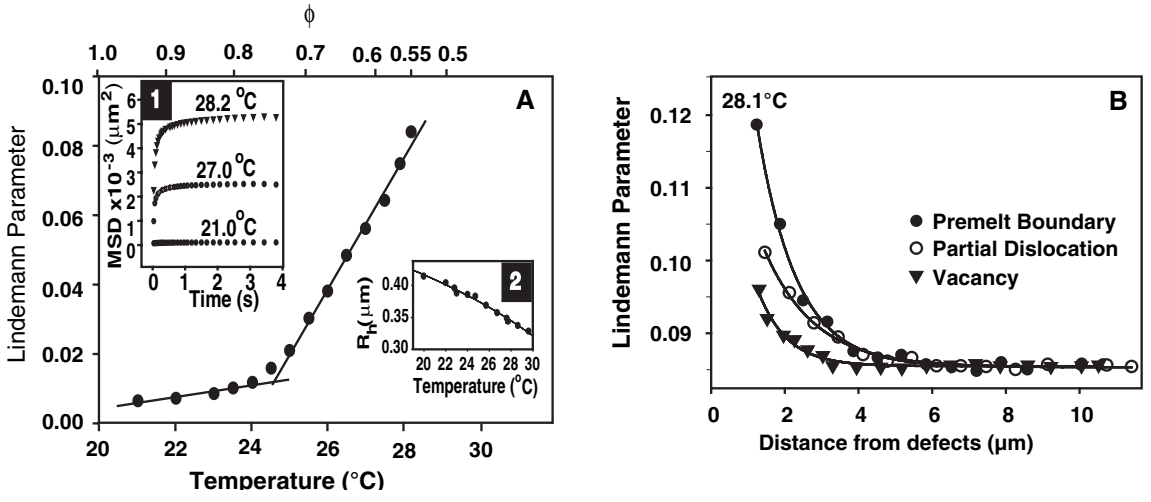

Fig. 4. (**A**) L as a function of colloidal crystal temperature (and computed particle volume fraction ϕ). These data are for regions far from defects. The curve exhibits a change in slope at 24.7°C. The crystal melts at 28.3°C, ϕ ~0.55. (Inset 1) Time evolution of 2D particle MSD; L is derived from the MSD plateau value. The error bars for ϕ, L, and temperature are 0.02, 0.004, and 0.1°C, respectively. (Inset 2) Measured microgel particle hydrodynamic radius R_h as a function of temperature. (**B**) The local L as a function of distance from a vacancy, a partial dislocation, and a melt front. Within 1 μm of the defects, the particle motion was too rapid and calculation of L was unreliable.

movement, so that the nearby particle fluctuations are large. Even the particles near isolated vacancies have large L, but the decay of L to bulk values is fastest from isolated vacancies.

Conclusions. We have demonstrated that premelting occurs at grain boundaries and dislocations located within colloidal crystals. These observations confirm an important mechanism for theories of melting. The amount of premelting depends on the nature of the interfaces and defects. Particle tracking has enabled us to study particle fluctuations both nearby and far from these defects in ways that are inaccessible to experimental probes of atomic crystals, revealing the excess free energy in these regions through higher values of L.

References and Notes

1. H. Lowen, *Phys. Rep.* **237**, 249 (1994).
2. J. G. Dash, *Rev. Mod. Phys.* **71**, 1737 (1999).
3. J. G. Dash, H. Fu, J. S. Wettlaufer, *Rep. Prog. Phys.* **58**, 115 (1995).
4. R. W. Cahn, *Nature* **413**, 582 (2001).
5. F. A. Lindemann, *Z. Phys.* **11**, 609 (1910).
6. S. F. Edwards, M. Warner, *Philos. Mag.* **40**, 257 (1979).
7. L. Burakovsky, D. L. Preston, R. R. Silbar, *Phys. Rev. B* **61**, 15011 (2000).
8. R. Lipowsky, *Phys. Rev. Lett.* **57**, 2876 (1986).
9. G. Ciccotti, M. Guillope, V. Pontikis, *Phys. Rev. B* **27**, 5576 (1983).
10. W. A. Curtin, *Phys. Rev. B* **39**, 6775 (1989).
11. B. Pluis, D. Frenkel, J. F. van der Veen, *Surf. Sci.* **239**, 282 (1990).
12. R. Ohnesorge, H. Lowen, H. Wagner, *Phys. Rev. E* **50**, 4801 (1994).
13. R. Lipowsky, U. Breuer, K. C. Prince, H. P. Bonzel, *Phys. Rev. Lett.* **62**, 913 (1989).
14. R. W. Cahn, *Nature* **323**, 668 (1986).
15. M. S. Pettersen, M. J. Lysek, D. L. Goodstein, *Phys. Rev. B* **40**, 4938 (1989).
16. U. Dahmen, S. Hagege, F. Faudot, T. Radetic, E. Johnson, *Philos. Mag.* **84**, 2651 (2004).
17. J. W. M. Frenken, J. F. van der Veen, *Phys. Rev. Lett.* **54**, 134 (1985).
18. J. F. van der Veen, *Surf. Sci.* **433-435**, 1 (1999).
19. B. Pluis, A. W. D. van der Gon, J. W. M. Frenken, J. F. van der Veen, *Phys. Rev. Lett.* **59**, 2678 (1987).
20. J. Q. Broughton, G. Gilmer, *Phys. Rev. Lett.* **56**, 2692 (1986).
21. S. Phillpot, J. F. Lutsko, D. Wolf, S. Yip, *Phys. Rev. B* **40**, 2831 (1989).
22. M. Stieger, J. S. Pedersen, P. Lindner, W. Richtering, *Langmuir* **20**, 7283 (2004).
23. J. Zhu *et al.*, *Nature* **387**, 883 (1997).
24. P. N. Pusey, W. van Megen, *Nature* **320**, 340 (1986).
25. S. B. Debord, L. A. Lyon, *J. Phys. Chem. B* **107**, 2927 (2003).
26. J. Wu, B. Zhou, Z. Hu, *Phys. Rev. Lett.* **90**, 048304 (2003).
27. A. M. Alsayed, M. F. Islam, A. G. Yodh, data not shown.
28. J. C. Crocker, D. G. Grier, *J. Colloid Interface Sci.* **179**, 298 (1996).
29. J. P. Hirth, J. Lothe, *Theory of Dislocations* (Wiley, New York, ed. 2, 1982).
30. P. Schall, I. Cohen, D. A. Weitz, F. Spaepen, *Science* **305**, 1944 (2004).
31. S. Pronk, D. Frenkel, *J. Chem. Phys.* **110**, 4589 (1999).
32. P. N. Pusey *et al.*, *Phys. Rev. Lett.* **63**, 2753 (1989).
33. J. Bongers, H. Versmold, *J. Chem. Phys.* **104**, 1519 (1996).
34. Y. N. Ohshima, I. Nishio, *J. Chem. Phys.* **114**, 8649 (2001).

35. We thank T. Lubensky, D. Discher, R. Kamien, E. Burstein, C. Crouch, and T. Sinno for useful discussions. This work was supported by NSF through grants DMR-0203378 and DMR-079909 (Materials Research Science and Engineering Center) and by NASA (NAG8-2172). P.J.C. acknowledges the support of the American Chemical Society Petroleum Research Fund.

Supporting Online Material

www.sciencemag.org/cgi/content/full/1112399/DC1
Movies S1 to S3

17 March 2005; accepted 24 May 2005
Published online 30 June 2005;
10.1126/science.1112399
Include this information when citing this paper.

Structure of a Synaptic γδ Resolvase Tetramer Covalently Linked to Two Cleaved DNAs

Weikai Li,[1] Satwik Kamtekar,[1] Yong Xiong,[1,2] Gary J. Sarkis,[1]* Nigel D. F. Grindley,[1] Thomas A. Steitz[1,2,3]†

The structure of a synaptic intermediate of the site-specific recombinase γδ resolvase covalently linked through Ser[10] to two cleaved duplex DNAs has been determined at 3.4 angstrom resolution. This resolvase, activated for recombination by mutations, forms a tetramer whose structure is substantially changed from that of a presynaptic complex between dimeric resolvase and the cleavage site DNA. Because the two cleaved DNA duplexes that are to be recombined lie on opposite sides of the core tetramer, large movements of both protein and DNA are required to achieve strand exchange. The two dimers linked to the DNAs that are to be recombined are held together by a flat interface. This may allow a 180° rotation of one dimer relative to the other in order to reposition the DNA duplexes for strand exchange.

Enzymes that catalyze site-specific recombination rearrange DNA in all three kingdoms to integrate, excise, or invert DNA segments for a variety of biological purposes. Site-specific recombinases are classified into the tyrosine and serine recombinase families, and the detailed mechanisms by which they achieve specific recombination are gradually emerging (*1*).

The γδ resolvase is a 20.5-kD transposon-encoded enzyme that belongs to the resolvase-invertase family of serine recombinases and catalyzes a recombination between two 114–base pair (bp) sites (*res*) that are arranged in the same orientation on negatively supercoiled circular DNA, resulting in the formation of two catenated DNA molecules. Each *res* site contains three different subsites, which are called sites I, II, and III, and each subsite binds a resolvase dimer (Fig. 1A). Six resolvase dimers and two *res* sites assemble into a higher-order structure called the synaptosome. Resolvase dimers bound at sites II and III of the two *res* sites initiate the formation of this assembly and activate the resolvase dimers bound at site I for synapsis, strand cleavage, strand exchange, and religation (*2*). Cleavage is achieved by a transesterification reaction that covalently links the Ser[10] (S10) residue of each subunit to a 5′ phosphate at the center of site I, freeing the 3′ hydroxyl group of the adjacent nucleotide (*3*, *4*). While covalently linked to the protein, the strands are exchanged with a resulting net 180° rotation (*5*–*7*). The four rearranged ends are then joined by an attack of the free 3′ hydroxyl groups on the phosphoserine linkages.

Several crystal structures of wild-type γδ resolvase have been determined, including a domain containing the active site (*8*, *9*), the full-length protein (*10*), and a resolvase dimer complexed with a site I DNA analog (*11*). γδ resolvase has an N-terminal catalytic domain followed by an extended α-helical arm (the E helix) and a C-terminal DNA binding domain. Two states of the molecules have been captured in these structures. First, crystals of the unliganded γδ resolvase identify one interface that promotes the formation of a dimer via the E helices and a second higher-order interdimer interface (termed the 2-3′) that is essential for *res* site synapsis (*8*–*10*, *12*, *13*). Second, the structure of a wild-type γδ-resolvase dimer complexed with a 34-bp analog of site I (*11*) captures a state before synapsis. In this structure, both catalytic S10 residues are distant from the scissile phosphates of the site I DNA, which is consistent with the inability of the wild-type protein to cleave linear DNA containing only a site I sequence.

Two models have been proposed for the structure of the synaptic tetramer bound at site I and the consequent strand-exchange mechanisms (*10*, *11*, *14*). In one model, two site I DNAs are held in close proximity inside a protein scaffold (*10*, *11*), whereas in the other they lie outside of a protein core and are separated by more than 50 Å (*10*, *11*, *14*). The DNA inside model was initially appealing because the DNA strands could be exchanged through subtle movements of the protein and the DNA at the cleavage sites, analogous to those subsequently observed with the tyrosine recombinase Cre (*15*). However, DNA phasing experiments

[1]Department of Molecular Biophysics and Biochemistry, and [2]Department of Chemistry, Yale University, and [3]Howard Hughes Medical Institute, New Haven, CT 06520, USA.

*Present address: 454 Life Sciences, 20 Commercial Street, Branford, CT 06405, USA.
†To whom correspondence should be addressed. E-mail: eatherton@csb.yale.edu